A viscoelastic earthquake cycle model for Taiwan

K. M. Johnson[1] and P. Segall

Department of Geophysics, Stanford University, Stanford, California, USA

S. B. Yu

Institute of Earth Sciences, Academia Sinica, Taipei, Taiwan

[1]   While recent geophysical measurements, including Global Positioning System (GPS) surveys, have clarified the mechanisms of active mountain building in the Taiwan arc-continent collision, the geometry of faults beneath the island remains unclear. In this paper we use GPS data collected before the 1999 Chi-Chi earthquake to image the geometry of active faults under Taiwan and estimate slip rates on these faults. We invert the data using kinematic and mechanical earthquake cycle models consisting of faulting in an elastic lithosphere overlying a viscoelastic asthenosphere. In the kinematic model, uniform slip is prescribed on the faults at a constant rate, while in the mechanical model, the faults slip in response to shear stresses in the lithosphere. These models explain the essential features of both the horizontal and vertical GPS velocity fields. We find a 27–39 km thick elastic lithosphere overlying a viscoelastic asthenosphere with Maxwell relaxation time of 15–80 years, or viscosity of 0.5–4×10^{19} Pa s. The models produce a combined slip rate of 30–50 mm/yr on the frontal thrusts in western Taiwan and 60–80 mm/yr of slip on the Longitudinal Valley Fault. Inversion of the data using both models indicates a décollement dipping $\sim 10°$ under western Taiwan and increasing in dip by no more than $10°$ under the Central Ranges and eastern Taiwan.

Citation: Johnson, K. M., P. Segall, and S. B. Yu (2005), A viscoelastic earthquake cycle model for Taiwan, *J. Geophys. Res.*, *110*, B10404, doi:10.1029/2004JB003516.

1.   Introduction

[2]   The ongoing Taiwan orogeny is occurring in the active collision zone between the Luzon arc of the Philippine Sea plate and the continental margin of the Eurasian plate (Figure 1). The Philippine Sea plate is converging at a rate of 70–80 mm/yr relative to Eurasia, with most of the shortening occurring within the width of the island of Taiwan [*Yu et al.*, 1997]. The active deformation front surfaces on land in western Taiwan and is characterized primarily by folds over blind faults. The active Chelungpu/Chukou thrust fault is located east of the deformation front. The Longitudinal Valley fault, which is the suture between the Philippine and Eurasian plates, is an active, steeply dipping reverse fault with oblique motion.

[3]   The mechanism of active mountain building in the Taiwan arc-continent collision has been debated for some time, with the debate centered on the unknown geometry of faults at depth. It was proposed by *Davis et al.* [1983] that Taiwan is forming as a thin accretionary wedge over a gently dipping décollement underlying the entire island.

This has largely been the paradigm for the last several decades. *Wu et al.* [1997], however, argued against this hypothesis, citing extensive geophysical evidence that the deformation in Taiwan involves the entire lithosphere. More recently, *Carena et al.* [2002] used a clustering algorithm and relocated seismicity to identify active fault planes highlighted by microseismicity. They interpret the microseismicity as revealing a nearly flat décollement underlying western Taiwan that steepens to as much as $45°$ under eastern Taiwan.

[4]   The collision process is being recorded by GPS instruments in a dense array of over 140 campaign and continuous sites, which provide horizontal and vertical velocities (Figure 2) [*Yu et al.*, 1999, 2001]. Figure 2 shows the GPS velocities averaged over the observation period 1992–1998. The velocities are relative to Penghu which is an island located about 50 km off the west coast of Taiwan on the relatively stable Chinese continental margin. There is a large gradient in horizontal velocity across the Longitudinal Valley fault zone on the east coast, indicating a high rate of strain accumulation. The velocity gradient is lower west of the Longitudinal Valley fault, including the location of the 1999 Chi-Chi earthquake, which ruptured the segment of the Chelungpu fault highlighted in red in Figure 2. The vertical velocity field shows uplift of 5–10 mm/yr in southern Taiwan and subsidence of up to 10 mm/yr on the east coast near the Longitudinal Valley fault. While there is

---

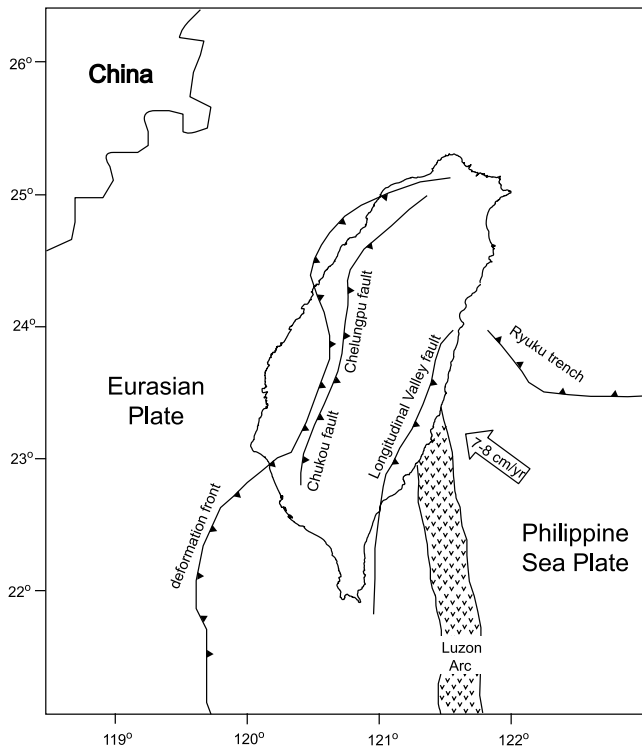[1]Now at Department of Geological Sciences, Indiana University, Bloomington, Indiana, USA.

Figure 1. Simplified tectonic setting of Taiwan. Eurasian plate subducts under the Philippine Sea plate south of Taiwan, and the Philippine Sea plate subducts under the Eurasian plate in northern Taiwan.

currently subsidence along much of the eastern coast, this area is known to have uplifted at rates of 5–10 mm/yr over the Holocene (Figure 2d)) [e.g., *Wang and Burnett*, 1990].

[5] *Hsu et al.* [2003] used the horizontal GPS data to estimate the fault geometry and slip rates in central Taiwan using an elastic dislocation model (Figure 3). In this model, the Earth is approximated as an elastic half-space, and the surface velocity field is attributed to steady creep on buried dislocations. They showed that the horizontal data are best explained with a shallow dipping (2°–11°) décollement underlying the entire island, much like the wedge geometry originally proposed for Taiwan. The vertical GPS data, however, cannot be explained with this elastic model. The model predicts uplift along the entire profile across Taiwan, and in particular does not match the observed subsidence on the east and west coasts and within the Longitudinal Valley. As suggested by *Hsu et al.* [2003], this misfit in the vertical velocities may be attributed to unmodeled inelastic deformation in the lower crust and upper mantle.

[6] We analyze the GPS data using kinematic and mechanical models, derived by K. Johnson and P. Segall (Kinematic and mechanical models of deformation in convergent plate boundary zones, submitted to *Journal of Geophysical Research*, 2005, hereinafter referred to as Johnson and Segall, submitted manuscript, 2005), that incorporate elastic deformation in the upper crust and viscous flow in the lower crust and upper mantle. Uniform slip is prescribed on the faults at a constant rate in the kinematic model, whereas the faults slip in response to shear stresses in the lithosphere in the mechanical model. We show that both the kinematic and mechanical models

reproduce the observed horizontal and vertical deformation patterns. In particular, the models resolve the dilemma of subsidence along the east and west coasts of Taiwan which cannot be explained by a purely elastic model. We demonstrate that the subsidence of the east and west sides of the island can be explained as a result of flexure of the elastic crust and associated viscous flow in the lower crust due to previous large earthquakes. We also show that the geometry of the active faults under Taiwan can be resolved with both the kinematic and mechanical models.

2. Tectonic Setting and Research Questions

[7] The geometry of the faults under Taiwan is not well known, but a schematic cross section (Figure 4) shows some of the possible subsurface features. Reflection profiles across the Western Foothills in the northern profile [*Hung and Suppe*, 2002] and balanced cross sections [*Suppe*, 1987] suggest that the frontal thrust faults flatten into a subhorizontal décollement at around 8–10 km depth. Analysis of GPS data from the 1999 Chi-Chi earthquake showed that slip likely occurred on the décollement during and following the earthquake [*Johnson and Segall*, 2004; *Hsu et al.*, 2002]. The shape of the continuation of this fault surface underneath the Central Ranges is still debated.

[8] There is no direct evidence for the west dipping Central Range fault as shown in Figure 4, however, a similar feature has been imaged in seismic profiles of the accretionary prism just south of Taiwan [*Lundberg*, 2003], and the steep topography on the east side of the Central Ranges is suggestive of a west dipping fault. *Willet and Brandon* [2002] and *Ding et al.* [2001] include a similar west dipping Central Range fault in numerical models of the orogenic process in Taiwan.

[9] The shape of the Longitudinal Valley fault in the vicinity of city of Taitung (Figure 2a) has been inferred from relocated seismicity by *Chen and Rau* [2002]. They imaged a listric fault that dips about ∼60° near the ground surface and shallows to perhaps ∼20° at about 25 km depth, as we have shown schematically in Figure 4.

[10] Bathymetric images show an east facing submarine fault scarp located about 40–50 km off the east coast of Taiwan [*Malavieille et al.*, 2002]. The scarp likely resulted from movement on a west dipping reverse fault. This west dipping fault is depicted in Figure 4 east of the Longitudinal Valley fault, however the geometry of this fault as shown is completely speculative.

[11] Large, M > 7.0, earthquakes in Taiwan since 1683 [*Tsai*, 1985] are concentrated on the east and west sides of the island (Figure 5). Two M = 7.1 earthquakes occurred on the Longitudinal Valley fault in 1951, generating surface rupture near the towns of Hualien and Chishang [*Bonilla*, 1975; *Cheng et al.*, 1996]. The 1951 earthquake near Chishang was composed of two shocks, one which initiated at about 16 km depth and the other at 36 km depth [*Cheng et al.*, 1996]. The three earthquakes in 1811, 1815 and 1882 were near the east coast of Taiwan but their epicenters and fault planes are unknown. The proposed epicenters in Figure 5 suggest either the Longitudinal Valley fault or the offshore westward dipping fault likely ruptured during the earthquakes, but based on the large uncertainty in the epicentral regions, there is no reason to rule out the
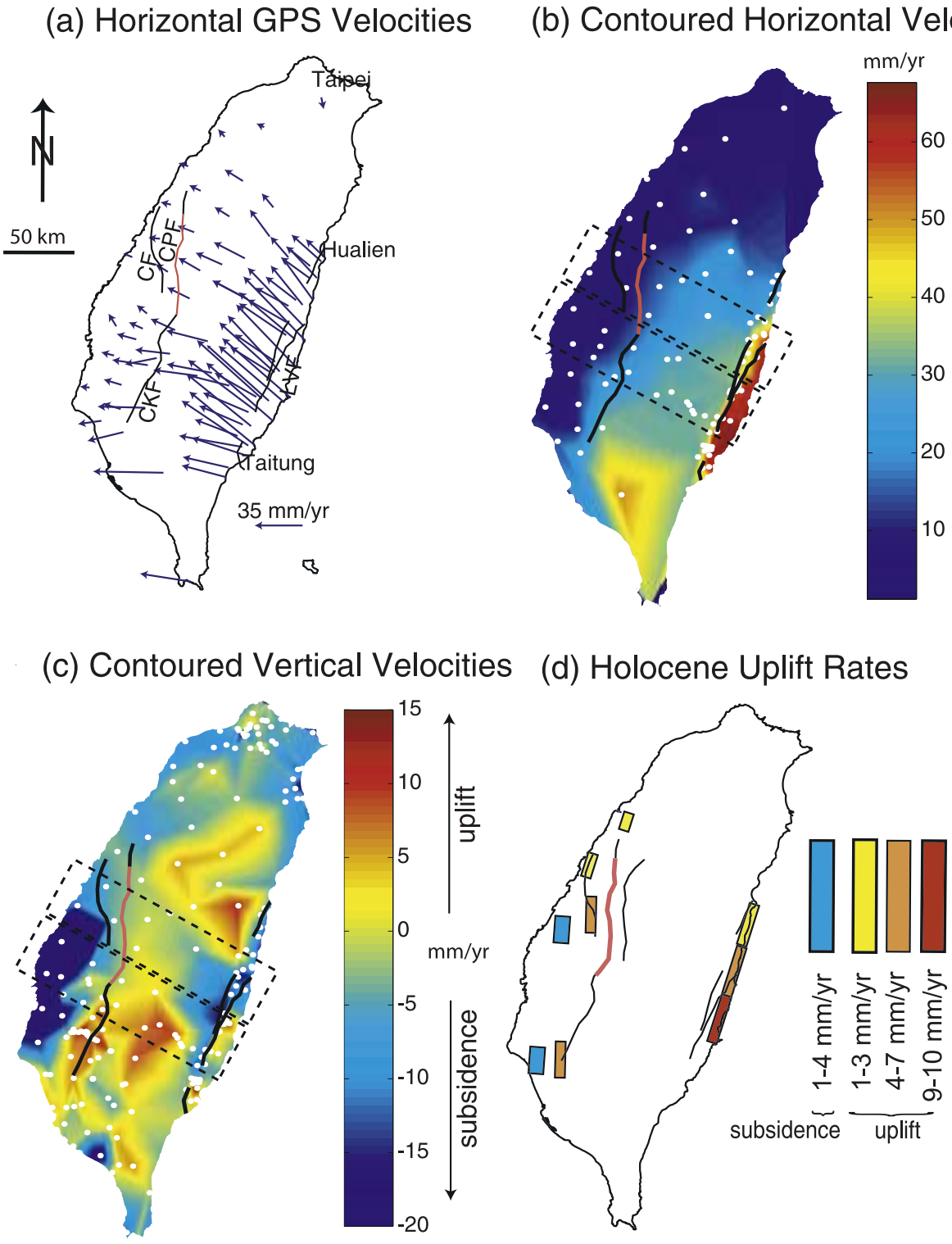
Figure 2. (a) Horizontal GPS velocity vectors. CF, Changua Fault; CPF, Chelungpu Fault; CKF, Chukou Fault; LVF, Longitudinal Valley Fault. Red line indicates extent of ground ruptures from 1999 Chi-Chi earthquake. (b) Contoured horizontal GPS velocities. (c) Contoured vertical GPS velocities. (d) Holocene uplift rates compiled from various studies [*Delcaillau et al.*, 1998; *Lai et al.*, 2002; *Bonilla*, 1975]. White dots in Figures 2b and 2c show location of GPS measurements used to generate contour plot.
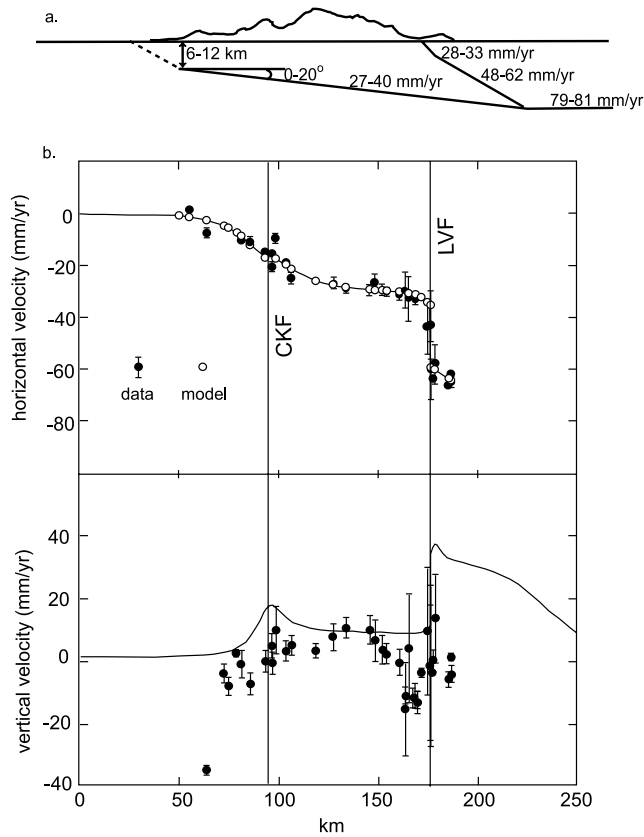
Figure 3. (a) Optimized fault geometry of *Hsu et al.* [2003] using elastic dislocation model. (b) Fit to horizontal and vertical data using elastic dislocation model. Note that only horizontal data were used in the optimization.

possibility that the Central Range fault ruptured during at least one of these earthquakes.

[12] In this paper we focus on the current deformation pattern in central Taiwan. Figure 6 shows the projection of GPS data in the dashed boxes in Figure 2 onto profiles oriented roughly perpendicular to the trend of the major faults and roughly parallel to the plate motion. The northern profile includes the section of the Chelungpu fault that ruptured during the 1999 M_w = 7.6 Chi-Chi earthquake. The profiles also cross the Chukou, Changua, and the Longitudinal Valley faults, all of which have been active during the
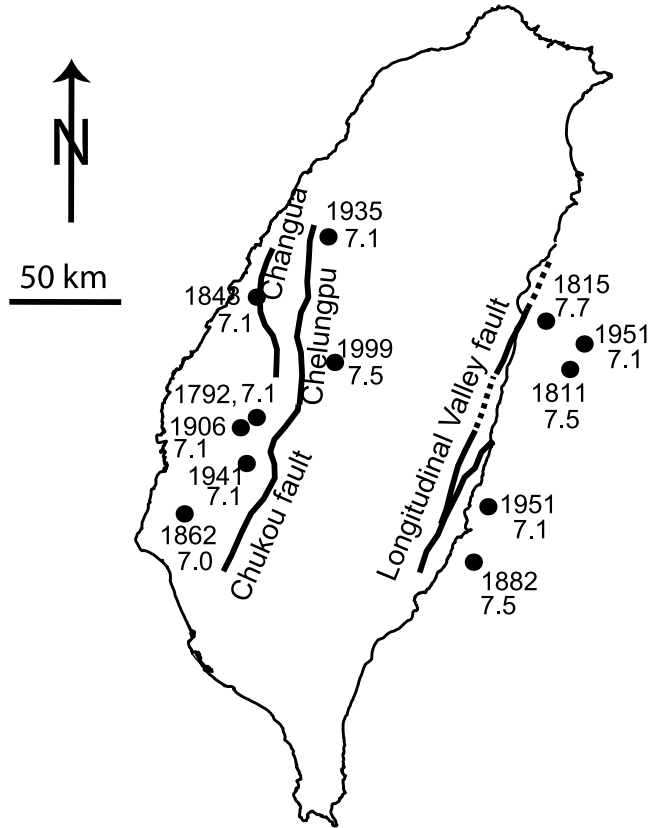

Figure 5. Active faults and approximate hypocenters of historical earthquakes [*Tsai*, 1985; *Bonilla*, 1975].

Holocene (Figure 5). The gradual gradient in horizontal velocity from the frontal thrusts in the west to the Longitudinal Valley fault in the east is observable in both profiles. There is a steep gradient in the horizontal and vertical velocities across the Longitudinal Valley in the northern profile. In the southern profile, the velocities are discontinuous across the Longitudinal Valley fault, consistent with observations of surface creep at this location [e.g., *Angelier et al.*, 1997]. Subsidence on the east coast and within the Longitudinal Valley is clear in both profiles. The eastern Central Ranges are uplifting about 5–10 mm/yr in the southern profile, but there is no significant uplift of the Central Ranges in the northern profile.
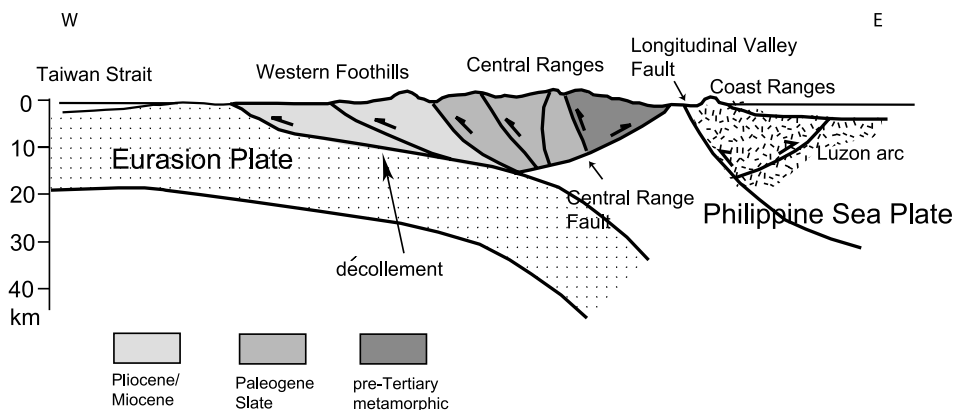

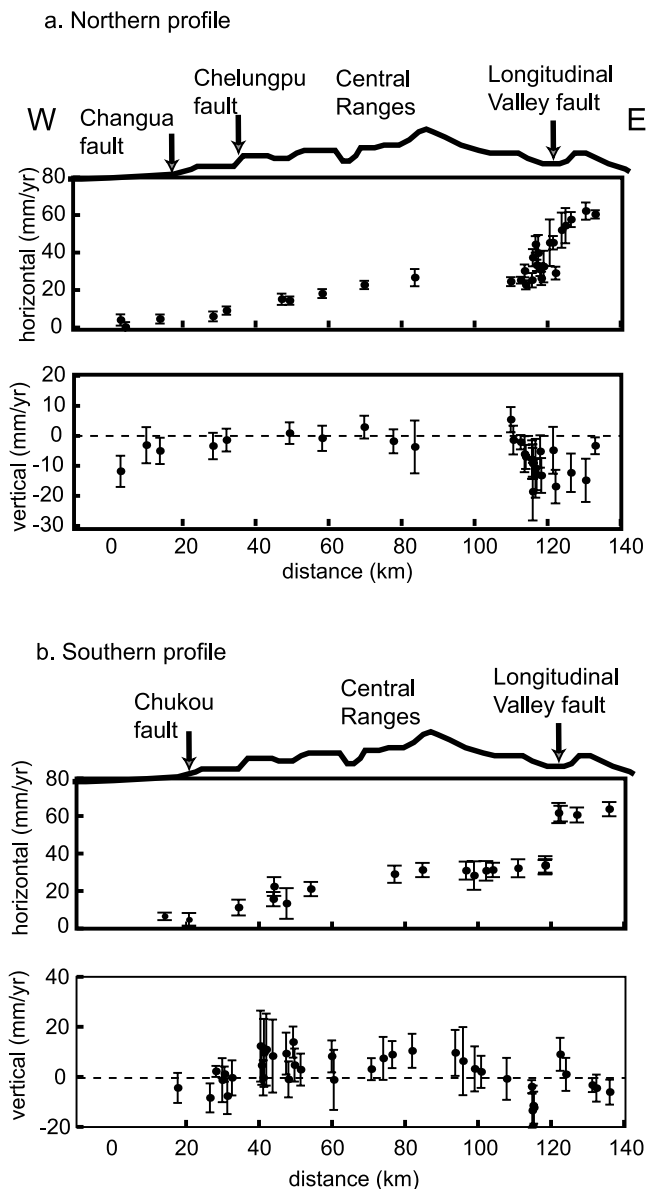**Figure 4.** Schematic cross section across Taiwan.

Figure 6. Horizontal and vertical velocities in central Taiwan projected onto profiles. Error bars are 2σ uncertainties.

[13] We use viscoelastic earthquake cycle models and the GPS data to address the following questions: (1) Can lithospheric plate flexure and corresponding viscous flow in the lower crust account for the vertical velocity patterns? (2) Is there an active décollement under the Central Ranges, and if so, what is the geometry? (3) Is there an active west dipping Central Range fault? (4) What are the slip rates on the various active faults? We begin with a kinematic model in which slip is prescribed on the faults. We then analyze the data with a mechanical model in which slip on the faults is driven by shear stresses in the lithosphere.

3. Kinematic Viscoelastic Earthquake Cycle Model

[14] We model deformation in Taiwan with faults in an elastic upper crust overlying a Maxwell viscoelastic lower

crust and mantle. We choose to model a viscous lower crust and mantle based partly on the result of *Hsu et al.* [2003], which showed that an entirely elastic Earth model cannot explain the vertical velocity patterns. Others have shown that an earthquake cycle model, consisting of faults with periodic earthquakes in an elastic lithosphere overlying a viscoelastic asthenosphere, can produce alternating patterns of subsidence and uplift throughout the cycle [e.g., *Thatcher and Rundle*, 1984; *Matsu'ura and Sato*, 1989]. To illustrate this, we show the velocity and displacement patterns in Figure 7 for a specified fault geometry and recurrence time. In this particular case, the model consists of a single 30° dipping reverse fault that is locked between earthquakes down to the middle of the elastic lithosphere. The fault slips uniformly at a constant rate below that depth. Sudden, uniform slip is imposed on the upper locked portion of the fault at intervals of $10t_R$, where t_R is the relaxation time of the asthenosphere, defined as $t_R = 2\eta/\mu$ where η is viscosity and μ is shear modulus. The fault is infinitely long in the direction of strike. A typical relaxation time is 30 years, so one can consider that the fault ruptures about every 300 years in this example. The horizontal velocities (Figure 7a) are higher than the convergent rate of $\cos(30°) = 0.48$ within 20H of the fault tip early in the earthquake cycle. Late in the cycle, the horizontal velocities within 20H of the fault tip are lower than the steady far-field convergence rate. The high rates after an earthquake are due to rapid flow in the viscous lower crust/upper mantle in response to the coseismic load induced by the earthquake. We can see from Figure 7d that the ground surface above the fault in the interval $0 < x < 2H$ subsides early in the earthquake cycle and uplifts later in the cycle, yet integrated over the whole earthquake cycle, the hanging wall uplifts in the interval $0 < x < 6H$. The alternating subsidence and uplift occurs in response to flexure of the elastic lithosphere as the asthenosphere flows in response to the stress load induced by the earthquake.

[15] Figure 8 shows the model geometry for central Taiwan and the various parameters to be estimated. For simplicity, we model the frontal faults in the Western Foothills as a single thrust fault. The two active thrusts are too closely spaced to resolve the individual slip rates. The frontal fault in the Western Foothills and the middepth section of the Longitudinal Valley fault (dashed lines) are assumed to be locked between earthquakes and slip periodically in large earthquakes at a specified recurrence interval determined from the historical earthquake record. The fault segments denoted with solid lines are assumed to creep continuously throughout the earthquake cycle at a constant rate.

[16] On the basis of the recent historical earthquake record discussed above (Figure 5), we assume a combined recurrence interval of 150 years for the frontal faults. On the basis of known subsurface geology in the Western Foothills, we assume the frontal fault dips 30° to the east into a 9° east dipping décollement. On the basis of evidence that coseismic slip and afterslip of the 1999 Chi-Chi earthquake occurred on the décollement [*Johnson and Segall*, 2004; *Hsu et al.*, 2002], we allow part of the décollement to be locked between earthquakes and rupture coseismically with the thrust. The transition from locked to creeping, labeled x_t in Figure 8, is estimated in the inversion. We also
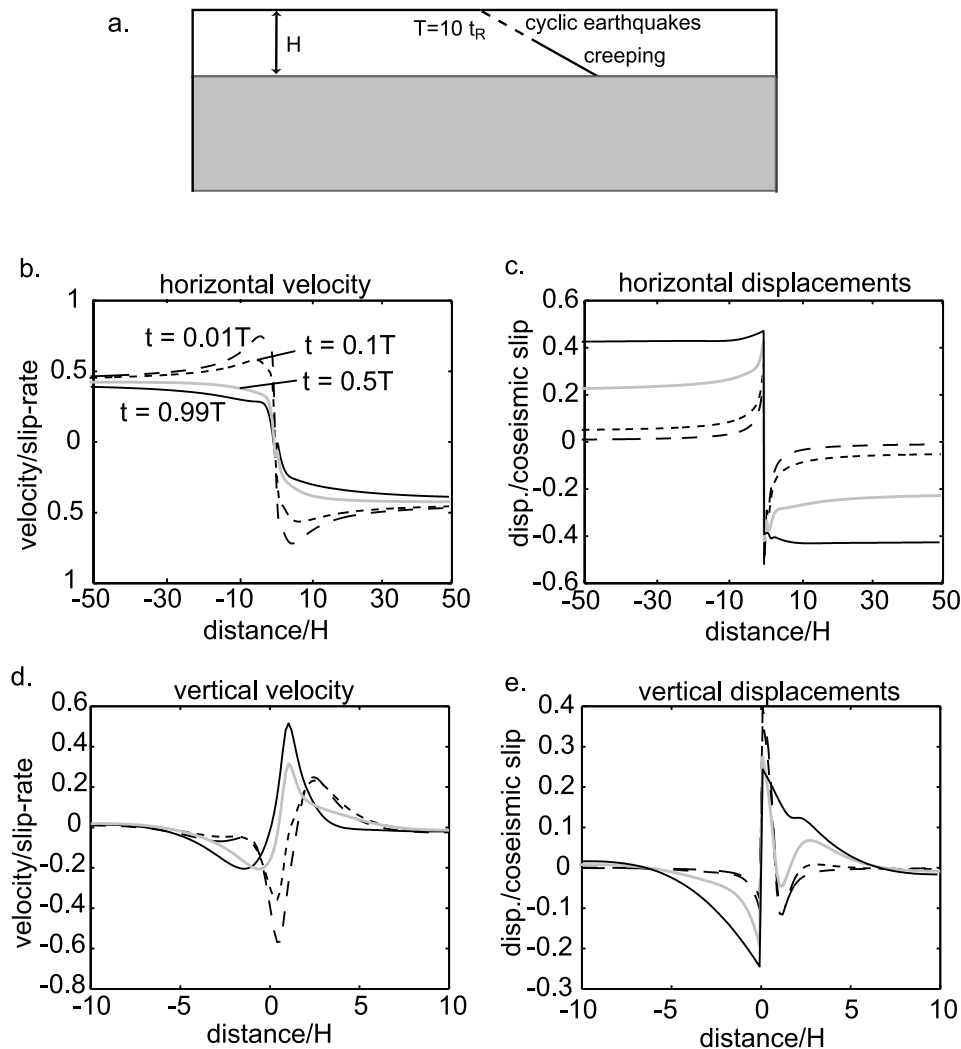
Figure 7. (a) Geometry of earthquake cycle model. Fault dips 30°. Upper half of fault slips in earthquakes with recurrence interval $T = 10t_R$, where t_R is the relaxation time, defined as twice the viscosity over the elastic shear modulus, $t_R = 2\eta/\mu$. Lower part of fault creeps at constant rate equal to the long-term rate on the upper part of the fault. (b–e) Velocities (horizontal, v_x, vertical, v_z) and displacements (horizontal, u_x, vertical, u_z) at four times during an earthquake cycle. Displacements are normalized by the magnitude of coseismic slip, Δu. Velocities are normalized by the coseismic slip divided by the recurrence time, T.

estimate the location, x_b, of the bend in the décollement and the dip, θ_1, of the eastern part of the décollement (segment 3, Figure 8).

[17] The geometry of the Longitudinal Valley fault is assumed based on relocated earthquakes, which reveal a listric fault shape [*Chen and Rau*, 2002]. We assume the upper part of the Longitudinal Valley fault (segment 5, Figure 8) is creeping based on the recognition that near surface creep would produce high strain rates, as observed in the GPS data. Furthermore, sections of the Longitudinal Valley fault are known to creep at the ground surface in southern Taiwan [e.g., *Angelier et al.*, 1997]. For simplicity, we assume that the upper creeping section breaks the ground surface as a discrete fault zone in both profiles, even though it is clear from the velocity profile in Figure 6a that the deformation is actually distributed over a 10 km wide zone in the northern profile. The depth to the bottom

of the creeping section is chosen arbitrarily at 10 km for this analysis. It turns out that the kinematic inversion is not sensitive to the depth of the bottom of the shallow creeping section. Likewise, the bottom of the locked section of the Longitudinal Valley fault is chosen arbitrarily as the bend in the fault. On the basis of the historical record of earthquakes on the Longitudinal Valley fault, we model the middepth section (segment 6, Figure 8) of the fault as locked interseismically and rupturing in earthquakes every 150 years in the northern profile and every 75 years in the southern profile. The upper part (5) is also permitted to slip periodically in earthquakes at the same time as rupture on the middepth section, with the constraint that the creep rate and the earthquake slip rate on (5) sum to the slip rate on (6). This is based on the observation that both 1951 earthquakes on the Longitudinal Valley fault ruptured the ground surface [*Bonilla*, 1975]. The lower part of the
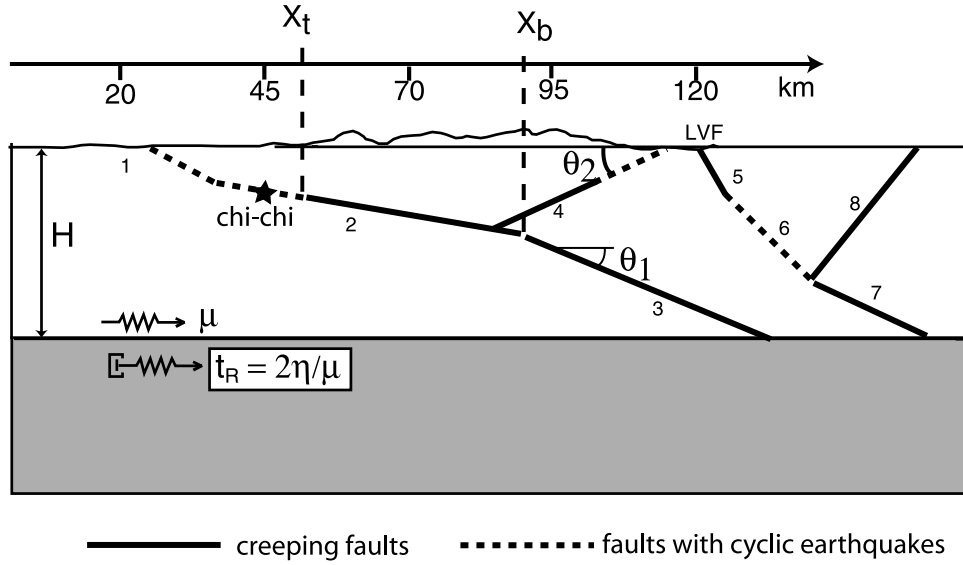
Figure 8. Model parameters. Fault segments are numbered 1–8. Fault parameters to be estimated are H, elastic thickness; t_R, relaxation time; x_t transition from locked to creeping; x_b, horizontal location of bend in detachment; θ_1, dip of segment 3; θ_2, dip of segment 4.

Longitudinal Valley fault is assumed to creep throughout the earthquake cycle.

[18] Because of a lack of historical earthquake information, the entire offshore fault (8) is assumed to creep throughout the earthquake cycle. The bottom half of the Central Range fault (4) is assumed to creep, and the upper half is assumed to be locked interseismically with periodic earthquakes. We estimate the repeat time and the time since the last earthquake on the Central Range fault.

[19] We also estimate the thickness of the elastic crust and the relaxation time of the viscoelastic lower crust and mantle. We expect the elastic thickness and relaxation time should not vary significantly from the northern to southern profiles, so we assume the parameters are the same in both profiles. We therefore perform a joint inversion of the data in both profiles for all the unknown parameters. In order that there not be excess long-term strain accumulation in the model, we place additional constraints on slip rates at fault intersections. It is assumed that the slip rate is continuous across the intersection of two fault segments. We also assume the scalar sum of the slip rates on faults 2 and 4 is equal to the slip rate on 3, and we assume the slip rates on faults 6 and 8 sum to the slip rate on fault 7. In total there are twelve parameters to estimate from the GPS data.

3.1. Monte Carlo Inversion Method

[20] To obtain a complete inversion for the model parameters of interest, we must get the joint probability distribution of the parameters. The model parameters are nonlinearly related to the surface velocities so there is no analytical means to obtain the joint probability distribution. Instead, we discretely sample the distribution using a Monte Carlo random walk with a Metropolis-Hastings step [e.g., *Mosegaard and Tarantola*, 2002]. We have a functional relationship between the vector of model parameters, **m**, and the vector of data, **d**,

$$\mathbf{d} = g(\mathbf{m}). \tag{1}$$

The a posteriori probability density function of the model parameters, σ, given the constraint by the data is

$$\sigma(\mathbf{m}|\mathbf{d} = g(\mathbf{m})) = k\rho_M(\mathbf{m})\rho_D(g(\mathbf{m})), \tag{2}$$

where k is a constant, ρ_M is the a priori probability density function for the model parameters, and ρ_D is the probability density function of the model parameters given only the information from the data [*Mosegaard and Tarantola*, 2002].

[21] We do not assume any prior information on the parameters of interest, so the a priori distribution is uniform. To sample the a posteriori distribution, σ, we initiate a random walk through the model space. The random walk is a so-called Markov Chain random walk in which the probability of visiting the model $\mathbf{m}_j$, given that the current model is $\mathbf{m}_i$, depends only on $\mathbf{m}_i$ and not on previously visited models. The model $\mathbf{m}_j$, with n unknowns, is generated randomly from $\mathbf{m}_i$ as follows

$$\mathbf{m}_j = \mathbf{m}_i + \sum_{k=1}^{n} \alpha_k r_k \mathbf{e}_k, \tag{3}$$

where r_k is a $(-1, 1)$ uniform random deviate, $\mathbf{e}_k$ is the unit vector along the kth axis in parameter space, and α_k scales the step size along coordinate directions and is determined empirically as discussed below. Undisturbed, this random walk simply samples the a priori distribution. To sample the a posteriori distribution, the random walk is directed with a so-called Metropolis step. The walk moves from $\mathbf{m}_i$ to $\mathbf{m}_j$ with probability

$$P_{ij} = \min\left(1, \frac{\rho_D(g(\mathbf{m}_j))}{\rho_D(g(\mathbf{m}_i))}\right). \tag{4}$$

If the model $\mathbf{m}_j$ is not accepted, a new random step is generated from $\mathbf{m}_i$.
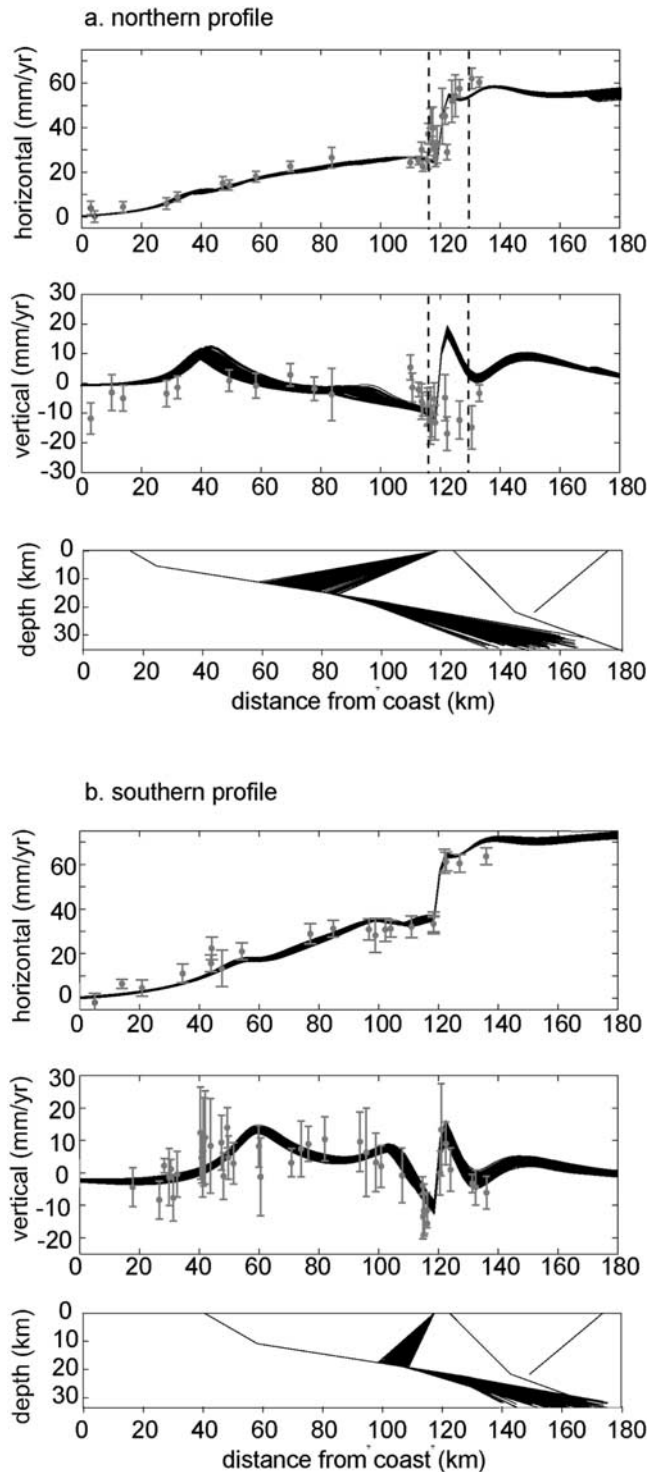
Figure 9. Fit to data and best fitting fault geometry for the kinematic inversions. Data between the vertical dashed lines were not used in the inversion.

[22] We have found if α_k is too large, randomly generated models are accepted at a low rate and the algorithm is inefficient. If α_k is too small, the random walk may spend too much time in a local minima and not adequately explore the high probability regions of the parameter space. Therefore, to select α_k, we start the inversion with an exploratory

stage in which we generate the random walk with large values of α_k. We then sequentially reduce α_k until the acceptance rate is at about 25–50%. The models from the exploratory stage are not kept. Once the acceptance rate reaches 25–50%, we stop reducing the size of α_k and begin keeping the models to build the posterior distributions.

3.2. Results and Discussion of Kinematic Inversion

[23] The fit to the data and the estimated fault geometry are shown in Figure 9. All of the models produced by the Monte Carlo random walk are plotted to show the distributions of model geometry and predicted velocities. The 95% confidence intervals on the slip rates are shown in Figure 10. The posterior distributions of all the parameters are shown in Figures 11, 12, and 13.

[24] In the northern profile, we excluded the GPS data in the interval $x = 115–130$ (dashed lines, Figure 9) because the velocities in that interval appear to be the result of distributed deformation, while we have chosen to model slip on a discrete fault surface. Most of the velocities lie within the 2σ uncertainties, with the exception of the overpredicted vertical velocities east of the Longitudinal Valley fault, particularly in the northern profile and the underpredicted vertical velocities west of the Longitudinal Valley fault in the northern profile. The model does not reproduce the steep gradient in the vertical velocities west of the Longitudinal Valley fault in the northern profile where the velocity increases from −20 mm/yr to about 10 mm/yr over a 10 km distance. However, the model does predict the more gentle gradient in vertical velocity west of the Longitudinal Valley fault in the southern profile. It is possible that the steep gradient in the northern profile is somehow related to the three-dimensional effects of northward subduction of the Philippine Sea plate, and so the large misfit may be a result of the 2D assumption. Shallow creep on the west dipping Central Range fault may increase the gradient in vertical velocities and improve the fit to the data, however, as far as we know, there is no independent evidence of creep at the
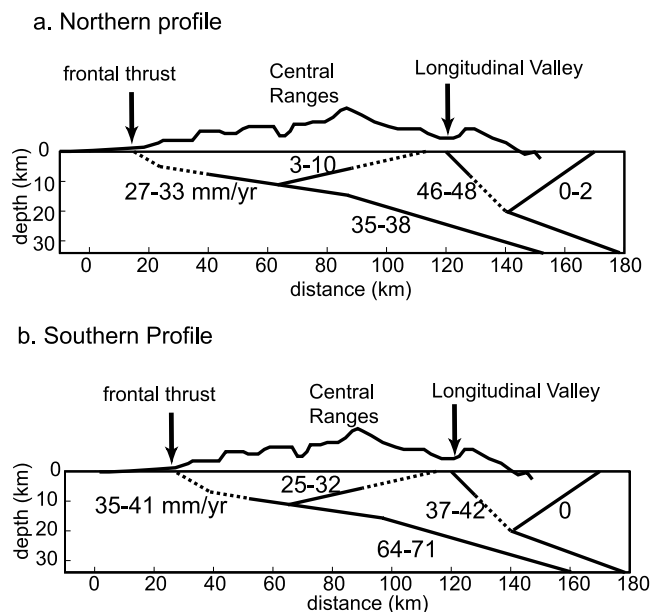

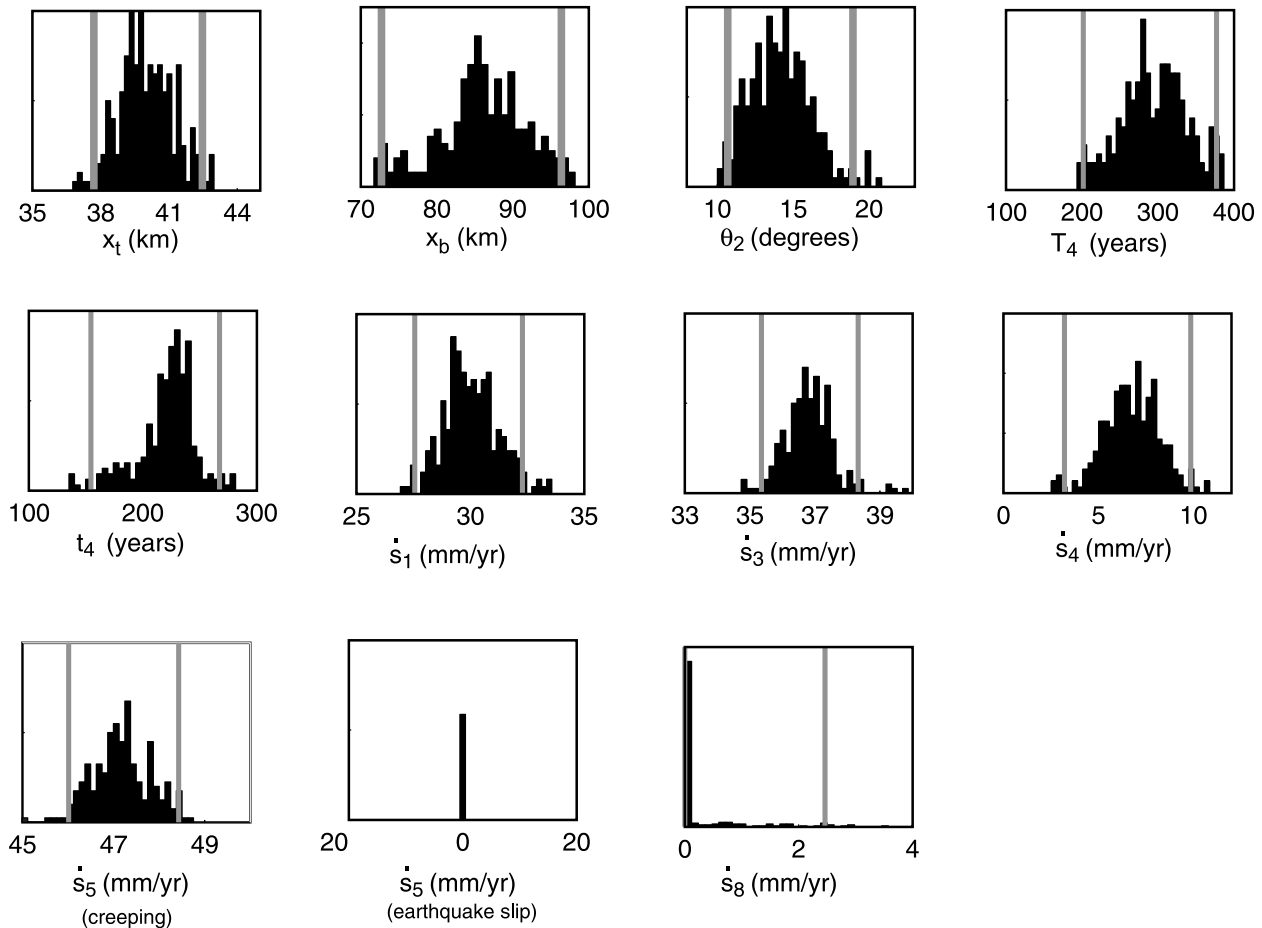**Figure 10.** The 95% confidence intervals in slip rates.

Figure 11. A posteriori distributions of the model parameters for the northern profile. The parameters x_t, x_b, and θ_2 are defined in Figure 8; s_i refers to slip rate on the ith fault as defined in Figure 8. T_4 and t_4 denote recurrence time and time since last earthquake, respectively, on fault 4. Gray vertical bars show 95% confidence limits.

ground surface in this location. Note, that unlike the entirely elastic model, the general trends of east and west coast subsidence are predicted by this model, especially in the southern profile (compare with Figure 3).

[25] The geometry of the décollement is well resolved as indicated by the narrow distribution in predicted fault geometries in Figure 9. The 10° dipping décollement under western Taiwan increases by more than 10° under eastern Taiwan, dipping in the range 10–20°.

[26] The slip rate on the Central Range fault is quite low in the northern profile (3–10 mm/yr) and relatively high in the southern profile (25–32 mm/yr). However, as we show in section 5, it is possible to fit the data qualitatively equally well without slip on the Central Range fault. The slip rate on the Longitudinal Valley fault is in the range 37–48 mm/yr which is similar to the combined slip rate on the frontal thrusts in the south and about 50% higher than the slip rate on the northern frontal thrusts. The northern frontal thrusts slip 27–33 mm/yr and the southern frontal thrust slip 35–41 mm/yr. At a 150 year recurrence interval, this results in 4.1–5.0 m of coseismic slip on the northern frontal thrusts, which is in reasonable agreement with the 5–6 m of average slip during the 1999 Chi-Chi earthquake. A 150 year recurrence interval on the northern profile Longitudinal

Valley fault results in 6.9–7.2 m of coseismic slip, and a 75 year recurrence interval on the Longitudinal Valley fault in the southern profile results in 2.8–3.2 m of coseismic slip. The two 1951 earthquakes each produced 2–3 m of slip at the ground surface [*Bonilla*, 1975], but the amount of slip at depth is unknown. Our inversion places no earthquake slip on the upper creeping part of the Longitudinal Valley fault in the northern profile and at most 1.5 m of slip during earthquakes (10 mm/yr averaged over the earthquake cycle) in the southern profile. There is not significant slip on the offshore west dipping fault (8) in the either profile.

[27] The relaxation time is resolved to within about a factor of 10 (Figure 13). Assuming an elastic shear modulus of 3 GPa, the viscosity of the asthenosphere is in the range $2.3–3.7 \times 10^{19}$ Pa s. The elastic thickness is resolved to within 5 km (27–32).

4. Mechanical Viscoelastic Earthquake Cycle Model

[28] A limitation of the kinematic model is that the fault slip does not arise naturally, but rather is imposed. Because slip is prescribed on the faults, the slip rates do not depend on the fault orientation relative to the local stress field and
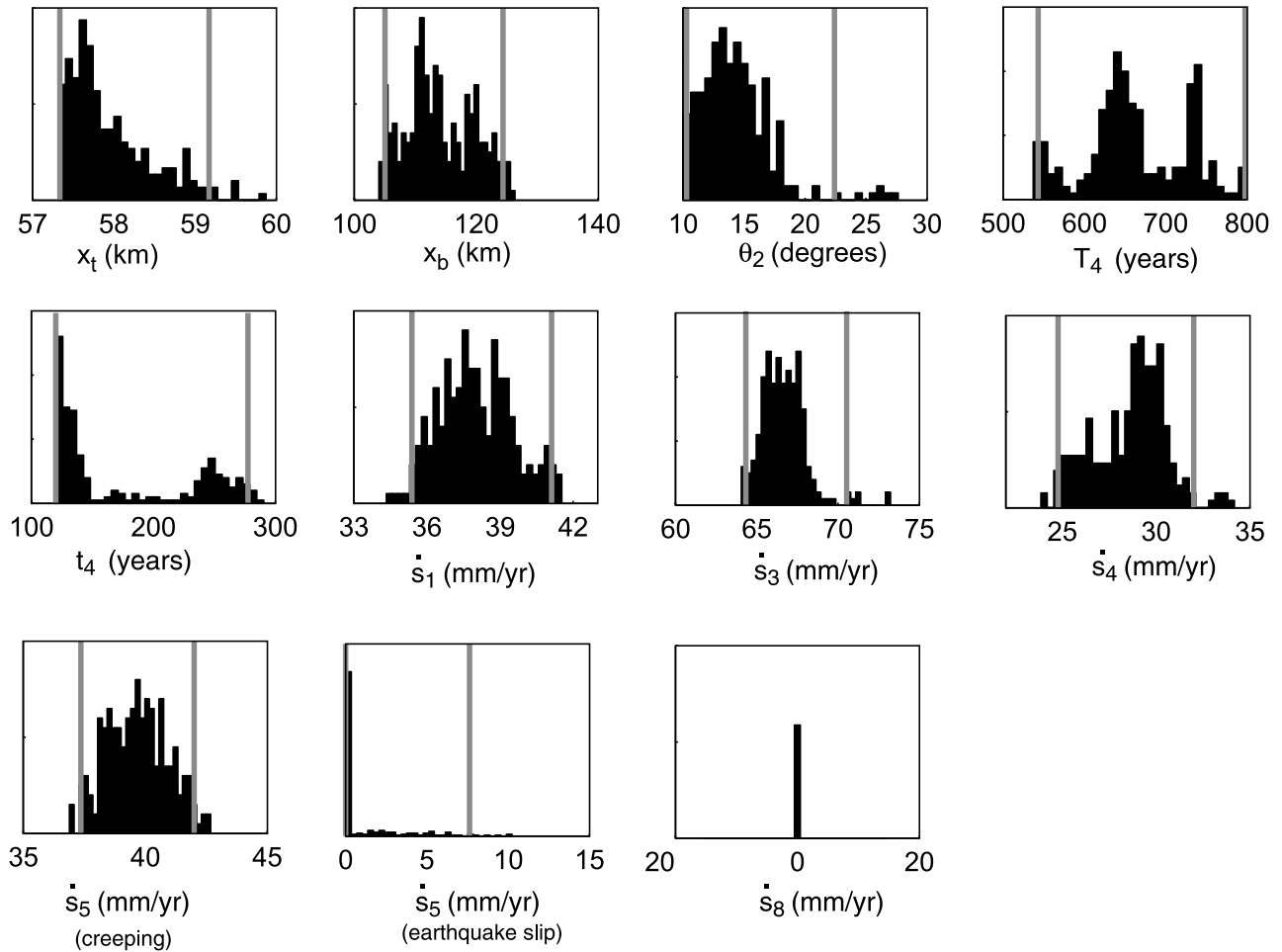
Figure 12. A posteriori distributions of the model parameters for the southern profile. See Figures 8 and 11 for explanation of model parameters.

there is no mechanical interaction between faults. Thus the slip rates and fault geometry obtained in the previous inversions are not necessarily mechanically consistent.

[29] In the mechanical model we apply a uniform far-field horizontal stress to the lithosphere (Johnson and Segall, submitted manuscript, 2005). The faults slip in response to the shear stresses on the faults induced by the far-field load and viscous flow in the lower crust. We apply the far-field driving stress to the elastic layer only; any load applied to the viscoelastic half-space produces flow that is decoupled from the elastic layer. Figure 14 illustrates the boundary conditions in this model. Solid lines indicate faults that creep throughout the earthquake cycle at constant resistive shear stress. Dotted lines indicate faults that are locked between earthquakes but slip with full stress drop during earthquakes. There is no frictional strength on the faults to dictate when failure occurs. The timing of earthquakes is prescribed. This model is constructed using a boundary element approach as discussed in detail by Johnson and Segall (submitted manuscript, 2005). The faults are discretized into patches of uniform slip and an earthquake cycle is discretized into 10 equal time increments.

[30] We now perform the Monte Carlo inversion using the mechanical model. There are six unknowns: (1) elastic thickness, H, (2) asthenosphere relaxation time, t_R,

(3) position of the dècollement bend, x_b, (4) dip of the eastern part of the dècollement, θ, (5) depth to the bottom of the upper creeping section of the Longitudinal Valley fault, D, and (6) the far-field driving stress, σ_{ff}. Because the kinematic inversion did not resolve significant amounts of slip on the Central Range fault in the northern profile or on the west dipping fault off the east coast, we do not include these faults in this inversion. The recurrence intervals and
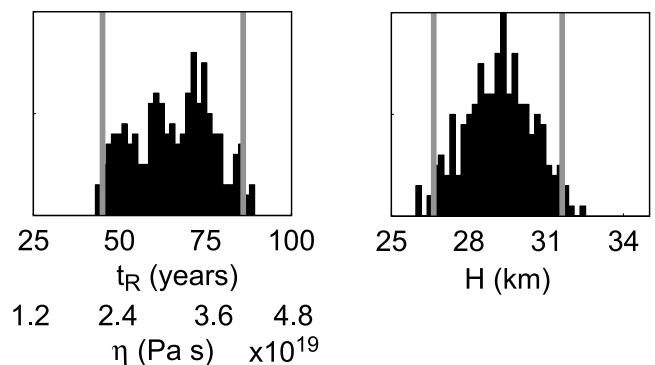

Figure 13. A posteriori distributions of elastic thickness and relaxation time for both profiles.
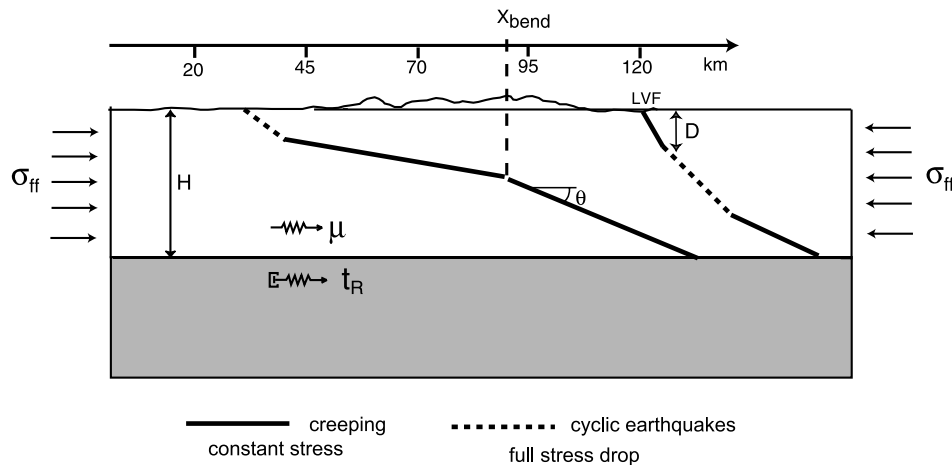
Figure 14. Mechanical model parameters. Fault parameters to be estimated: H, elastic thickness; t_R, relaxation time; x_b, horizontal location of bend in detachment; θ, dip of segment 3.

times since the last earthquakes are the same as in the kinematic model.

[31] The fit to the data and the resulting fault geometry are shown in Figure 15. As previously, the velocity profiles from all of the models produced in the Monte Carlo inversion are plotted. The fit to the data is qualitatively as good as the fit from the kinematic inversion. Most of the data are fit within the 95% confidence bars. The major difference between results of this inversion and the kinematic inversion is the resolution of the dècollement geometry. The dècollement dip is resolved to within about $2°$ and the location of the bend to within several kilometers. In the northern profile, the dècollement bends at about $x = 95$ km and then dips at about $18°$ into the asthenosphere. In the southern profile there is only a $3°$ change in the angle of the dècollement dip at about $x = 100$ km.

[32] The slip distributions are shown in Figure 16. For comparison, the 95% confidence limits on the slip rates from the kinematic inversion are represented by vertical bars. The slip rate during the observation period 1992–1998 varies considerably with depth in the mechanical model. The average contemporary slip rate over middepths along the frontal thrust/dècollement system is similar to the uniform slip rate obtained from the kinematic inversion, however the mechanical slip rate is higher in both profiles below 20 km depth. The depth-averaged mechanical model slip rate on the Longitudinal Valley fault system is similar to the uniform slip rates obtained from the kinematic inversion. The depth-averaged long-term slip rates on the frontal thrust/dècollement system from the mechanical model inversion is similar to the estimate from the kinematic inversion in the southern profile, while the mechanical model slip rate is $10–15$ mm/yr higher than in the mechanical model. In both profiles, the long-term slip rate on the Longitudinal Valley fault system is higher in the mechanical model inversion. This discrepancy is due to additional earthquake slip in the mechanical model. Averaged over the earthquake cycle there is $10–30$ mm/yr of earthquake slip, in addition to creep on the Longitudinal Valley fault in the mechanical model, while the kinematic inversion places minimal earthquake slip on the shallow creeping section.

[33] Figure 17 shows the a posteriori distributions of the depth to the bottom of shallow creep, D, elastic thickness,

H, and relaxation time, t_R. In both profiles, D is in the range $15–20$ km, about middepth of the elastic crust which is $34–39$ km thick. The relaxation time range of $5–50$ years is comparable to the range obtained from the kinematic inversion.

5. Uplift Rates Over the Holocene

[34] We now consider the long-term deformation pattern over many earthquake cycles. We approach this with caution, however, recognizing that the methodology employs a small strain approximation and is therefore only accurate for small amounts of deformation. Furthermore, the lithosphere is modeled as entirely elastic, while we know that the lithosphere exhibits permanent, inelastic deformation over times periods longer than an earthquake cycle.

[35] In Figure 18, the long-term uplift rates predicted by the kinematic model are shown along with the Holocene uplift rates determined from dated marine and fluvial terraces [*Delcaillau et al.*, 1998; *Lai et al.*, 2002] are shown with vertical bars. The long-term model rate is simply the total vertical displacement over an earthquake cycle, including the coseismic displacements, divided by the recurrence time. We see that the predicted uplift rates are generally consistent with the Holocene rates. The uplift rate is overpredicted on the east coast in the northern profile, but otherwise the predicted rates are consistent with measured values. Figure 19 compares the long-term uplift rates for the mechanical model with the Holocene data. The pattern is similar to the kinematic model, although the mechanical model does not produce uplift just west of the Longitudinal Valley in the southern profile because slip was not allowed on the Central Range fault.

[36] Although the long-term vertical velocity profiles from both models are locally consistent with the few available Holocene rates, there are significant discrepancies between the general pattern of theoretical uplift rates and the current topography of the island of Taiwan. The models predict long-term subsidence in the Central Ranges, where the current topography is highest. As far as we know, there are no geomorphic measurements of Holocene uplift rates in the Central Ranges to compare with the theoretical uplift rates, however, apatite fission track ages indicate long-term
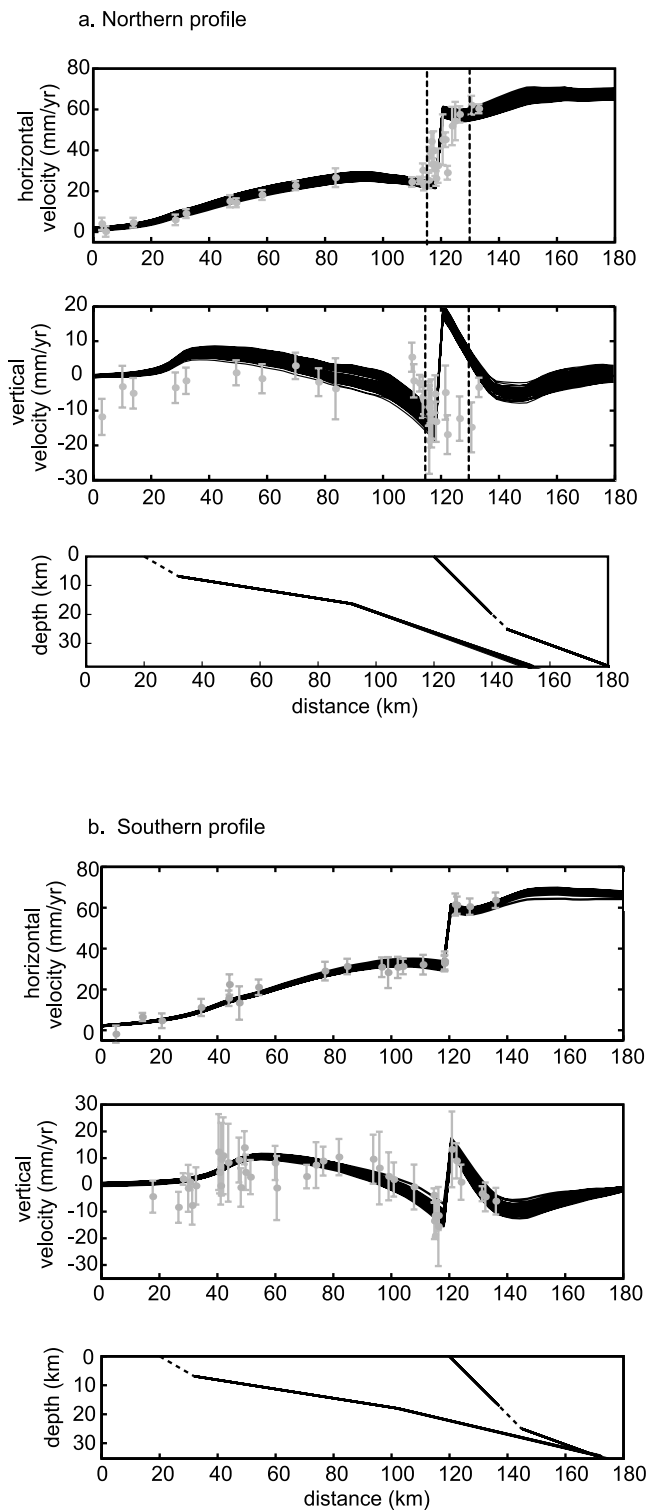
a. Northern profile

b. Southern profile

Figure 15. Fit to data and best fitting fault geometry for the mechanical model inversion. All models from the Monte Carlo inversion are plotted. Dashed lines in the bottom plots represent fault sections that are locked between earthquakes. Solid lines represent faults that creep at all times.

exhumation rates of 3–6 mm/yr over a much longer timescale in the Central Ranges [e.g., *Dadson et al.*, 2003]. The models predict the highest uplift rates in the Coastal Ranges, where the mountains are considerably lower than in the Central Ranges. Clearly, over timescales much longer than those represented by GPS data, the Central Ranges have been lifted up more than the Coast Ranges to the east. Thus, if the uplift predictions from this model are correct, the current uplift rate does not reflect the average uplift over the duration of the orogeny. Clearly slip on faults in the Central Ranges that were once active but appear to be currently inactive would generate uplift in the Central Ranges consistent with the high topography.

6. Discussion and Conclusions

[37] We have shown that the horizontal and vertical GPS velocity fields in central Taiwan, during the 1992–1998 time period leading up to the 1999 Chi-Chi earthquake, can be explained with an earthquake cycle model consisting of slip on faults in an elastic upper crust overlying a Maxwell viscoelastic lower crust/upper mantle.

[38] A Monte Carlo-Metropolis method was employed to invert the GPS data for fault geometry, slip rates, and lithospheric rheology. We performed inversions using both a kinematic model, in which spatially uniform slip is prescribed at a constant rate, and a stress-driven, mechanical model with frictionless faults. In the latter model the faults slip in response to an applied far-field horizontal compressional stress and local perturbations to the stress field caused by slip on faults and viscous flow in the asthenosphere.

[39] The inversions indicate a 27–39 km thick elastic lithosphere overlying a viscoelastic asthenosphere with Maxwell relaxation time of 15–80 years, or viscosity of $0.5–4 \times 10^{19}$ Pa s.

[40] The long-term slip rate on the Longitudinal Valley fault system is estimated to be 60–80 mm/yr using the mechanical model, substantially higher than the 37–48 mm/yr estimated using the kinematic model. The disagreement is due to additional earthquake slip on the creeping parts of the Longitudinal Valley fault in the mechanical model. *Shyu et al.* [2004] have published the only available paleoseismic slip rate estimates for the Longitudinal Valley fault. Using folded and dated fluvial terraces in the Coastal Ranges, east of the Longitudinal fault, they obtain a slip rate of ~22 mm/yr for the past 4,000 years (J. H. Shyu (personal communication, 2005); note this updated rate is lower than reported by *Shyu et al.* [2004]). This rate is lower than the shallow creep rate revealed by GPS data and creep meters [*Angelier et al.*, 1997] and our kinematic model estimate. The high Longitudinal Valley slip rate in our mechanical model should be interpreted with caution as it is likely an overestimate resulting from the 2D assumption of an infinitely long fault. In this 2D model, the Longitudinal Valley fault is locked at depth along the entire length of the fault. This locking stores up elastic stress that is relaxed during the earthquakes. It is quite possible that the amount of slip during earthquakes could be significantly reduced with a 3D model of the Longitudinal Valley fault in which the stuck patch has finite dimension along strike. In this case, more of the fault area would be able to creep between earthquakes and smaller amounts of slip would occur during earthquakes, perhaps reducing the total slip on the fault. We intend to explore 3D mechanical models in the future that may yield more realistic slip rates on the Longitudinal Valley fault.
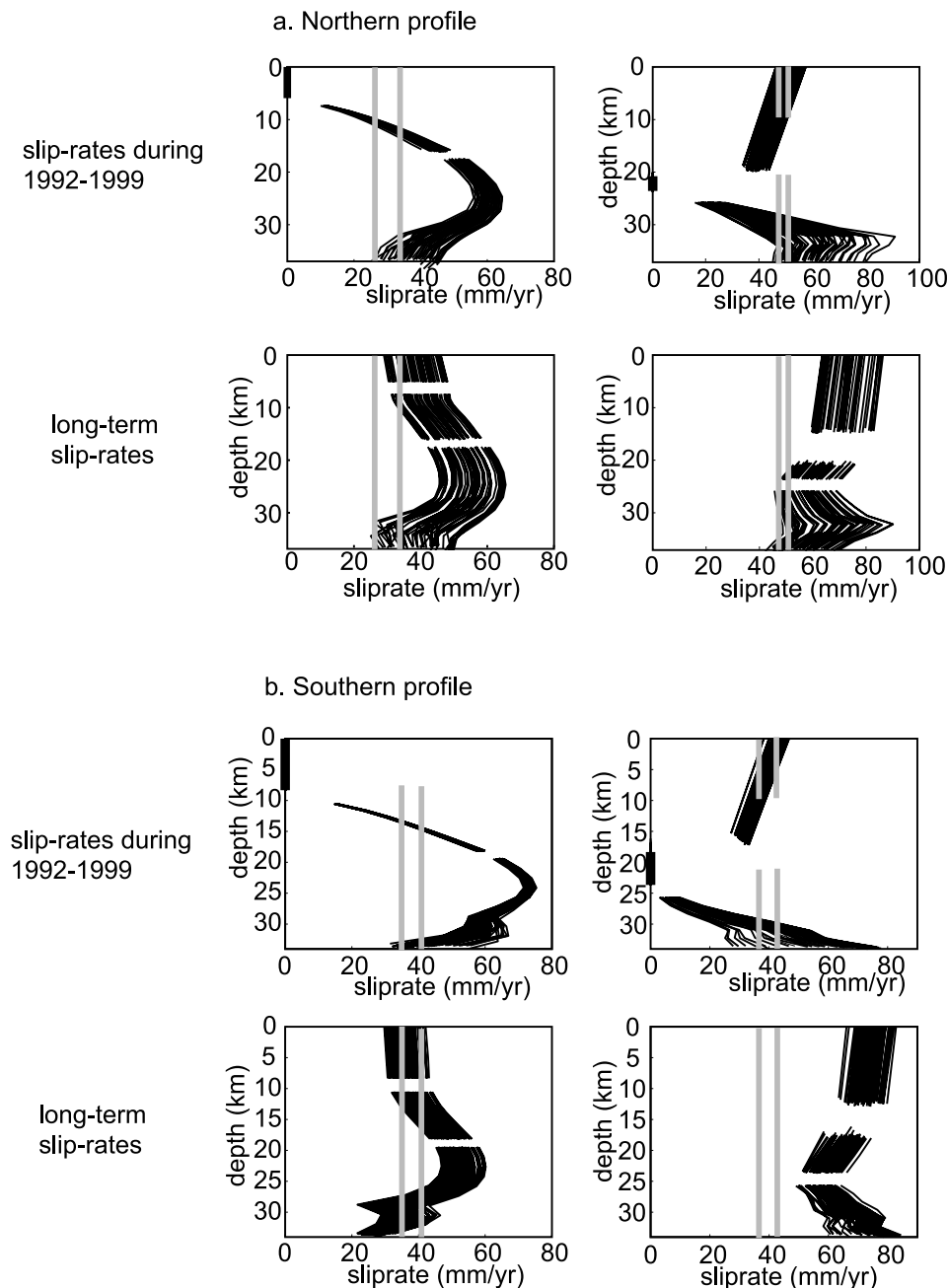
Figure 16. Slip rates plotted with depth along the fault. (left) Slip rates with depth along the thrust fault/dècollement system. (right) Slip rates with depth along the Longitudinal Valley fault system. Slip rates on each fault segment are separated with a gap. For comparison, vertical bars show 95% confidence interval in slip rate from kinematic inversion.

[41] The mechanical and kinematic long-term slip rate estimates on the frontal thrusts are in better agreement than the Longitudinal Valley fault slip rate estimates. The combined slip rate is in the range 30–50 mm/yr. We emphasize again that this an estimate of the combined slip rate of all active frontal thrust faults. As we mentioned earlier, individual slip rates on the closely spaced frontal thrust faults cannot be resolved with this model. At this time, published paleoseismic estimates of slip rates and recurrence times of earthquakes are available only for the Chelungpu fault. *Chen et al.* [2003] estimate a slip rate of about 8.5 mm/yr with an average recurrence interval of less than 700 years

for the last 1900 years at a trench cite located in the central section of the Chelungpu fault. *Wang* [2005] estimates lower slip rates of 3.8–5.8 mm/yr with average recurrence interval of 630 years for the southern Chelungpu fault and 1900 years for the northern part of the fault. All of these estimates of the average slip rate over the last four or so earthquakes are lower than the long-term slip rate on the Chelungpu fault. *Chen et al.* [2003] estimate an average long-term slip rate of 14–20 mm/yr for the entire 0.5–0.7 m.y. history of the Chelungpu fault, and *Lee et al.* [2001] estimate a long-term slip rate of 10–15 mm/yr. If the Chelungpu fault accommodates 10–20 mm/yr, then our
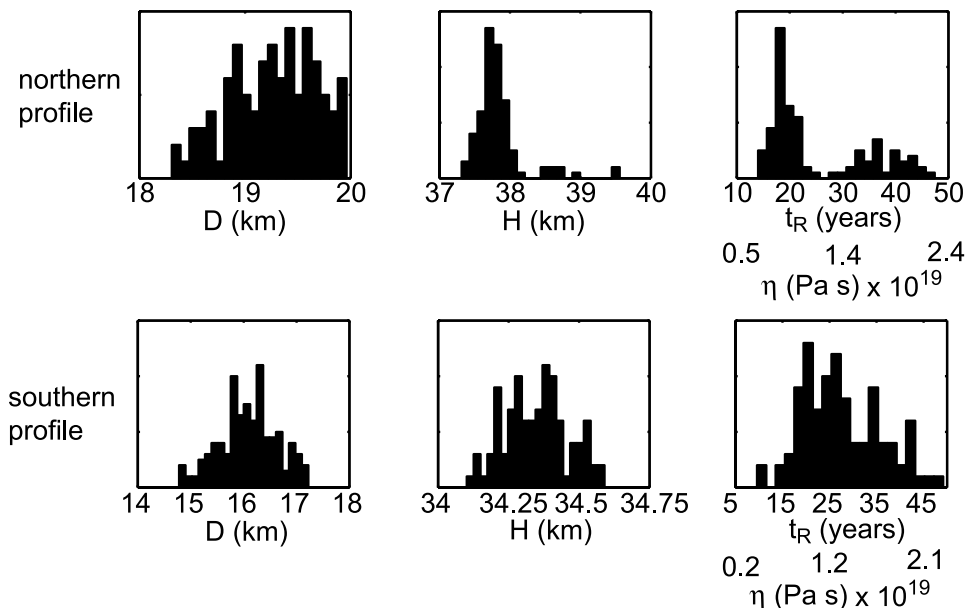
Figure 17. Monte Carlo inversion distributions of Longitudinal Valley fault locking depth, D, elastic thickness, H, and relaxation time, t_R.

modeling suggests the other active frontal thrusts must contribute a combined slip rate of 10–30 mm/yr. About 16 mm/yr of this slip can be attributed to the Changua fault [Simoes et al., 2004; M. Simoes, personal communication, 2005].

[42] The Central Range fault and offshore back thrust were not included in the mechanical model, but inversions using the kinematic model place 25–32 mm/yr of slip on the Central Range fault in the southern profile but negligible slip on the northern profile. There is negligible slip on the offshore back thrust in both profiles. As mentioned previously, there is no direct geophysical or geological evidence for the west dipping Central Range fault we have modeled although previous modeling efforts have included similar structures in numerical models. Our results clearly do not provide any clear evidence of a west dipping Central Range fault.

[43] The dècollement geometry is well resolved using both models. The dècollement dips 10° under the western Central Ranges and increases in dip by at most 10° under the eastern Central Ranges. The inversion results suggest, especially in the southern profile, that the dècollement may merge into the Longitudinal Valley fault at depth, forming a single master fault which might be interpreted as the subduction interface. The dècollement geometry is similar to the geometry suggested by Carena et al. [2002], who used relocated and collapsed seismicity to delineate potential faults. They suggest the dècollement dips gently under most of the island and steepens to 30–45° under the Longitudinal Valley. They also locate some more diffuse seismicity east of the Longitudinal Valley that might be related to Longitudinal Valley fault or the west dipping fault that surfaces off the east coast, but no clear faut geometry is delineated in this area.

[44] Long-term uplift rates obtained from the kinematic and mechanical models are generally consistent with Holocene uplift rates obtained from dated fluvial and coastal terraces. The current topography in Taiwan, however, is not mirrored by the model uplift patterns produced by slip on the frontal thrusts and the Longitudinal Valley fault. The

models predict long-term subsidence in the eastern Central Ranges where the current topography is highest. Using these simple models with faults in an elastic crust overlying a viscoelastic lower crust/upper mantle, additional slip on
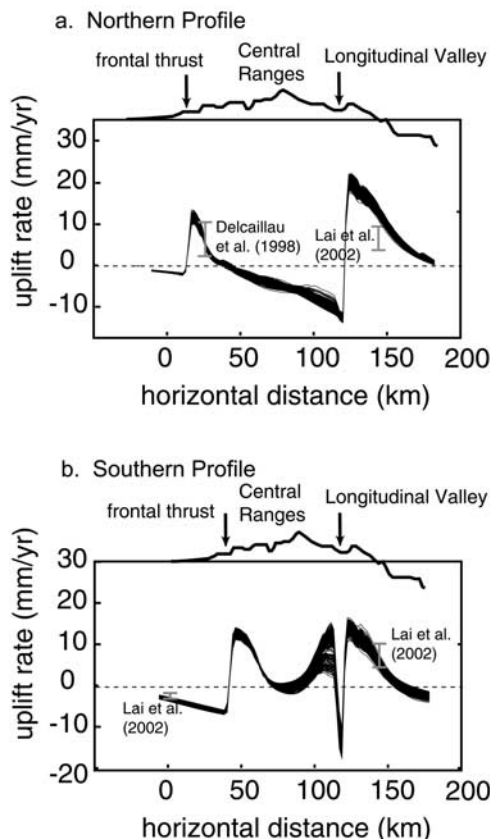

Figure 18. Long-term kinematic model uplift rates compared with estimates of Holocene rates from dated fluvial and wave-cut terraces.
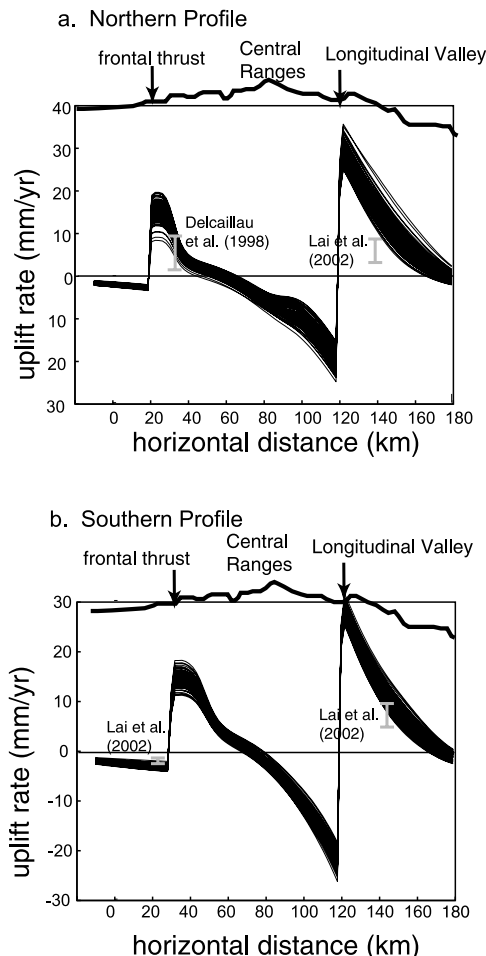
Figure 19. Long-term mechanical model uplift rates compared with estimates of Holocene rates from dated fluvial and wave-cut terraces.

faults within the Central Ranges and lower slip rates on the Longitudinal Valley fault would be necessary to produce the current topography.

References

Angelier, J., H. Chu, and J. Lee (1997), Shear concentration in a collision zone: Kinematics of the Chihshang fault as revealed by outcrop-scale quantification of active faulting, Longtiduinal Valley, eastern Taiwan, *Tectonophysics*, *274*, 117–143.

Bonilla, M. (1975), A review of recently active faults in Taiwan, *U.S. Geol. Surv. Open File Rep.*, *75-41*.

Carena, S., J. Suppe, and H. Kao (2002), Active detachment of Taiwan illuminated by small earthquakes and its control on first-order topography, *Geology*, *30*, 935–938.

Chen, H., and R. Rau (2002), Earthquake locations and style of faulting in an active arc-continent plate bouldary: The Chihshang fault of eastern Taiwan, *Eos Trans. AGU*, *83*(47), Fall Meet. Suppl., Abstract T61B-1277.

Chen, W., K. Lee, L. Lee, D. Ponti, C. Prentice, Y. Chen, H. Chang, and Y. Lee (2003), Paleoseismology of the Chelungpu fault during the past 1900 years, *Quat. Int.*, *115–116*, 167–176.

Cheng, S. N., Y. T. Yeh, and M. S. Yu (1996), The 1951 Taitung earthquake in Taiwan, *J. Geol. Soc. China*, *39*(3), 267–285.

Dadson, S. J., et al. (2003), Links between erosion, runoff variability and seismicity in the Taiwan orogen, *Nature*, *426*, 648–651.

Davis, D., J. Suppe, and F. Dahlen (1983), Mechanics of fold-and-thrust belts and accretionary wedges, *J. Geophys. Res.*, *88*, 1153–1172.

Delcaillau, B., B. Deffontaines, L. Foissac, J. Angelier, J. Deramond, P. Souquet, H. Chu, and J. Lee (1998), Mophotectonic evidence from lateral propagation of an active frontal fold: Pakuashan anticline, foothills of Taiwan, *Geomorphology*, *24*, 263–290.

Ding, Z. Y., Y. Yang, Z. Yao, and G. Zhang (2001), A thin-skinned colli-sional model for the Taiwan orogeny, *Tectonophysics*, *332*, 321–331.

Hsu, Y. J., N. Bechor, P. Segall, S. B. Yu, L. C. Kuo, and K. F. Ma (2002), Rapid afterslip following the 1999 Chi-Chi, Taiwan earthquake, *Geophys. Res. Lett.*, *29*(16), 1754, doi:10.1029/2002GL014967.

Hsu, Y., M. Simons, S. Yu, L. Kuo, and H. Chen (2003), A two-dimensional dislocation model for interseismic deformation of the Taiwan mountain belt, *Earth Planet. Sci. Lett.*, *211*, 287–294.

Hung, J., and J. Suppe (2002), Subsurface geometry of the Sani-Chelungpu faults and fold scarp formation in the 1999 Chi-Chi Taiwan earthquake, *Eos Trans. AGU*, *83*(47), Fall Meet. Suppl., Abstract T61B–1268.

Johnson, K. M., and P. Segall (2004), Imaging the ramp-decollement geo-metry of the Chelungpu fault using coseismic GPS displacements from the 1999 Chi-Chi, Taiwan earthquake, *Tectonophysics*, *378*, 123–139.

Lai, T., M. Hsieh, P. Liew, and Y. Chen (2002), Holocene rock uplift and subsidence in the coastal area of Taiwan, *Eos Trans. AGU*, *83*(47), Fall Meet. Suppl., Abstract T61B–1273.

Lee, J., Y. Chen, K. Sieh, K. Mueller, W. Chen, H. Chu, Y. Chan, C. Rubin, and R. Yeats (2001), A vertical exposure of the 1999 surface rupture of the Chelungpu fault at Wufeng, western Taiwan: Structural and paleo-seismic implications for an active thrust fault, *Bull. Seismol. Soc. Am.*, *91*(5), 914–929.

Lundberg, N. (2003), Surface processes in the accretionary prism south of Taiwan: Response to tectonic forcing and oceanic 'climate', *Geol. Soc. Am. Abstr. Programs*, *35*(6), 29.

Malavieille, J., et al. (2002), Arc-continent collision in Taiwan; new marine observations and tectonic evolution, *Spec. Pap. Geol. Soc. Am.*, *358*, 187–211.

Matsu'ura, M., and T. Sato (1989), A dislocation model for the earthquake cycle at convergent plate boundaries, *Geophys. J.*, *96*, 23–32.

Mosegaard, K., and A. Tarantola (2002), Probabilistic approach to inverse problems, in *International Handbook of Earthquake and Engineering Seismology*, pp. 237–265, Elsevier, New York.

Shyu, J., K. Sieh, J. Avouac, W. Chen, Y. Chen, and C. Lin (2004), Millenial slip rate of the Longitudinal Valley fault, a major element of Taiwan's tandem suturing, *Eos Trans. AGU*, *85*(47), Fall Meet. Suppl., Abstract T13F-07.

Simoes, M., J. Avouac, Y.-G. Chen, A. Singhvi, Y.-C. Chan, M. Jaiswal, and S. Bernard (2004), Investigating the kinematics of shortening across the Pakuashan anticline, west central Taiwan, *Eos Trans. AGU*, *85*(47), Fall Meet. Suppl., Abstract T13F-05.

Suppe, J. (1987), The active Taiwan mountain belt, in *The Anatomy of Mountain Ranges*, edited by J. P. Schaer and J. Rodgers, pp. 277–293, Princeton Univ. Press, Princeton, N. J.

Thatcher, W., and J. Rundle (1984), A viscoelastic coupling model for the cyclic deformation due to periodically repeated earthquakes at subduction zones, *Geophys. Res. Lett.*, *89*, 7631–7640.

Tsai, Y. (1985), A study of disastrous earthquakes in Taiwan, 1683–1895, *Bull. Inst. Earth Sci. Acad. Sin.*, *5*, 1–44.

Wang, C., and W. Burnett (1990), Holocene mean uplift rates across an active plate-collision boundary in Taiwan, *Science*, *248*, 204–206.

Wang, J. (2005), Earthquakes rupturing the Chelungpu fault in Taiwan are time predictable, *Geophys. Res. Lett.*, *32*, L06316, doi:10.1029/2004GL021884.

Willet, S. D., and M. T. Brandon (2002), On steady states in mountain belts, *Geology*, *30*, 175–178.

Wu, F., R. Rau, and D. Salzberg (1997), Taiwan orogeny: Thin-skinned or lithospheric collision?, *Tectonophysics*, *274*, 191–220.

Yu, S., H. Chen, L. Kuo, R. Punongbayan, and E. Ramos (1999), GPS observation of crustal motion in the Taiwan-Luzon region, *Geophys. Res. Lett.*, *26*, 923–926.

Yu, S. B., H. Y. Chen, and L. C. Kuo (1997), Velocity field of GPS stations in the Taiwan area, *Tectonophysics*, *274*(1–3), 41–59.

Yu, S. B., et al. (2001), Preseismic deformation and coseismic displacements associated with the 1999 Chi-Chi, Taiwan, earthquake, *Bull. Seismol. Soc. Am.*, *91*(5), 995–1012.

K. M. Johnson, Department of Geological Sciences, Indiana University, 1001 East 10th St., Bloomington, IN 47405, USA. (kaijjohns@indiana.edu)

P. Segall, Department of Geophysics, Stanford University, 397 Panama Mall, Stanford, CA 94305, USA. (segall@pangea.stanford.edu)

S. B. Yu, Institute of Earth Sciences, Academia Sinica, 128 Academia Road, Sec. 2, Nankang Taipei, 115, Taiwan. (eayusb@ccvax.sinica.edu.tw)